



LAWRENCE  
LIVERMORE  
NATIONAL  
LABORATORY

# South pole bang-time diagnostic on the National Ignition Facility

A. MacPhee, D. Edgell, D. K. Bradley, E. J. Bond, S. Burns, D. A. Callahan, J. Celeste, J. Kimbrough, A. J. Mackinnon, J. Magoon, M. J. Eckart, V. Glebov, D. Hey, G. Lacielle, J. Kilkenny, J. Parker, T. C. Sangster, M. J. Shoup, C. Stoeckl, T. Thomas

May 7, 2012

High-Temperature Plasma Diagnostics Conference  
Monterey, CA, United States  
May 6, 2012 through May 10, 2012

## **Disclaimer**

---

This document was prepared as an account of work sponsored by an agency of the United States government. Neither the United States government nor Lawrence Livermore National Security, LLC, nor any of their employees makes any warranty, expressed or implied, or assumes any legal liability or responsibility for the accuracy, completeness, or usefulness of any information, apparatus, product, or process disclosed, or represents that its use would not infringe privately owned rights. Reference herein to any specific commercial product, process, or service by trade name, trademark, manufacturer, or otherwise does not necessarily constitute or imply its endorsement, recommendation, or favoring by the United States government or Lawrence Livermore National Security, LLC. The views and opinions of authors expressed herein do not necessarily state or reflect those of the United States government or Lawrence Livermore National Security, LLC, and shall not be used for advertising or product endorsement purposes.

# South pole bang-time diagnostic on the National Ignition Facility<sup>a)</sup>

D. H. Edgell,<sup>1,b)</sup> D. K. Bradley,<sup>2</sup> E. J. Bond,<sup>2</sup> S. Burns,<sup>2</sup> D. A. Callahan,<sup>2</sup> J. Celeste,<sup>2</sup> M. J. Eckart,<sup>2</sup> V. Yu. Glebov,<sup>1</sup> D. S. Hey,<sup>2</sup> G. Lacaille,<sup>2</sup> J. D. Kilkenny,<sup>3</sup> J. Kimbrough,<sup>2</sup> A. J. Mackinnon,<sup>2</sup> J. Magoon,<sup>1</sup> J. Parker,<sup>2</sup> T. C. Sangster,<sup>1</sup> M. J. Shoup III,<sup>1</sup> C. Stoeckl,<sup>1</sup> T. Thomas,<sup>2</sup> and A. MacPhee<sup>2</sup>

<sup>1</sup>Laboratory for Laser Energetics, University of Rochester, Rochester, NY 14623-1299, USA

<sup>2</sup>Lawrence Livermore National Laboratory, Livermore, CA 94550, USA

<sup>3</sup>General Atomics, San Diego, CA 92121, USA

(Presented XXXXX; received XXXXX; accepted XXXXX; published online XXXXX)

(Dates appearing here are provided by the Editorial Office)

The south pole bang-time (SPBT) diagnostic views National Ignition Facility (NIF) implosions through the lower hohlraum laser entrance hole to measure the time of peak x-ray emission (peak compression) in indirect drive implosions. Five chemical-vapor-deposition (CVD) diamond photoconductive detectors (PCD's) with different filtrations and sensitivities record the time-varying x rays emitted by the target. Wavelength-selecting highly oriented pyrolytic graphite (HOPG) crystal mirror monochromators increase the x-ray signal-to-background ratio by filtering for 11-keV emission. Diagnostic timing and the *in-situ* temporal instrument response function are determined from laser impulse shots on the NIF. After signal deconvolution and background removal, the bang time is determined to 45-ps accuracy. The x-ray "yield" (mJ/sr/keV at 11 keV) is determined from the total area under the peak.

## I. INTRODUCTION

In the inertial confinement fusion concept,<sup>1</sup> energy is deposited on a target fuel capsule, ablating the surface and imploding the target mass inward. The implosion compresses and heats the fuel to ignition conditions. The National Ignition Facility (NIF)<sup>2</sup> at Lawrence Livermore National Laboratory (LLNL) has the goal of successfully igniting a fuel capsule. Implosions on the NIF currently use the indirect-drive approach<sup>3</sup> where laser energy irradiates the inside of a hohlraum, which strongly emits x rays. The x rays are absorbed by a capsule inside the hohlraum. To optimize target performance, it is essential to compare experimental measurements with the model predictions to understand the physical processes that occur during the implosion.

Near peak compression and temperature, the hot plasma inside the imploding capsule emits a burst of x rays with a full width at half maximum (FWHM) of the order of 100-200 ps. The x-ray bang time is defined as the time of the peak of this burst relative to the beginning of the laser pulse. Bang-time predictions depend sensitively on the simulation physics, including the energy absorbed in the capsule shell, the hydrodynamic response of the capsule, the radiation hydrodynamics of the compressed core plasma, etc. The accuracy of the bang-time predictions is a sensitive indicator of the accuracy of the implosion physics in the model.

The importance of diagnosing the x-ray bang time is evidenced by the multiple diagnostics existing or planned on the NIF designed to measure it: The gated x-ray detector (GXD),<sup>4</sup> the

hardened gated x-ray imager (hGXI),<sup>5</sup> the active readout in a neutron environment (ARIANE)<sup>6</sup>, and the streaked polar instrumentation for diagnosing energetic radiation (SPIDER)<sup>7</sup>. These diagnostics are designed to be deployed in implosions with different levels of neutron yields up to near-ignition.

This paper describes the fielding of a new simple and robust x-ray bang-time diagnostic<sup>8</sup> designed to operate over the full range of neutron yields on the NIF up to near-ignition levels of  $10^{18}$  neutrons (see Sec. II). The south pole bang-time (SPBT) diagnostic was developed collaboratively by the Laboratory for Laser Energetics (LLE) and LLNL.

The data processing and deconvolution applied to the SPBT signals are described in Sec. III. Details of the analysis of x-ray timing shots and typical NIF implosions are explained in Secs. IV and V, respectively.

## II. DIAGNOSTIC DESIGN

The SPBT consists of five differently filtered chemical-vapor-deposition (CVD) diamond photoconductive detectors (PCD's)<sup>9</sup> shielded in a diagnostic head (see Fig. 1). Four of the PCD's are arranged to detect monochromatic x rays reflected by x-ray mirrors (see below). The fifth detector intended for broadband x-ray and neutron measurements is centrally located and views the target directly. Each PCD channel has individual filters located in their entrance holes. By filtering the channels differently and using PCD's with different sensitivities, SPBT can measure capsule x rays over a range of intensities from current levels to those anticipated during ignition shots.

CVD diamond PCD's were selected for their robustness and response time. CVD diamonds can survive the high neutron yields of NIF implosions. Their response times are sufficient to resolve the time-dependent x-ray flux and measure the x-ray bang time to within tens of picoseconds. While CVD diamond PCD's

<sup>a)</sup>Contributed (or Invited) paper published as part of the Proceedings of the 19th Topical Conference on High-Temperature Plasma Diagnostics, Monterey, California, May, 2012.

<sup>b)</sup>Author to whom correspondence should be addressed: email@none.edu.

are sensitive to both x rays and neutrons, the signals are separated by 40 ns due to their relative speeds and can be easily discriminated.

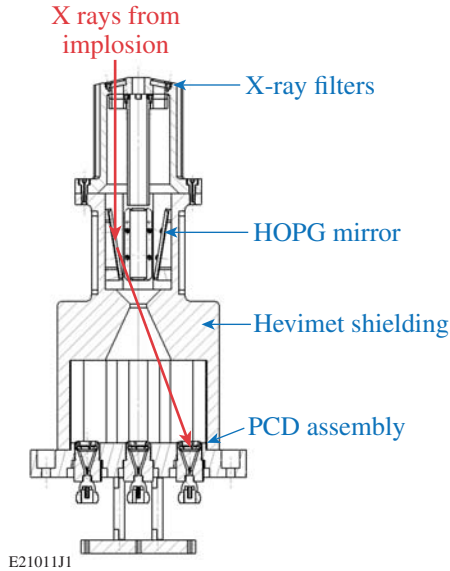


FIG 1. A diagram of the south pole bang-time (SPBT) diagnostic head shows the layout of the photoconductive detectors (PCD's) and highly oriented pyrolytic graphite (HOPG) mirrors. The red arrows illustrate one of the x-ray pathways from an entrance hole to a PCD.

An individual detector assembly, shown in Fig. 2, is a modification of an original design of Glebov.<sup>10</sup> In our design, 50- $\Omega$  impedance is maintained over the transition from the cable center conductor to the diamond surface by using a coaxial Macor dielectric disk and a 15- $\mu\text{m}$ -thick electrode on the diamond lower surface. This eliminates a ringing observed near the peak of the detector impulse response function.

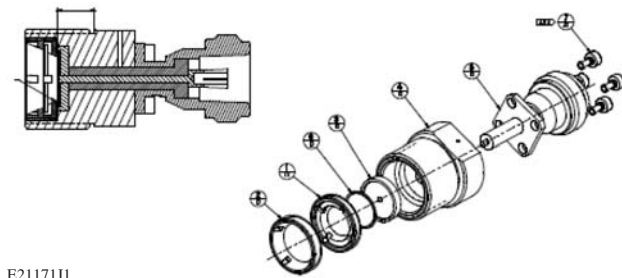


FIG 2. PCD assembly. The Macor disk along with the 15- $\mu\text{m}$ -thick gold electrode sputter deposited on the diamond bottom maintain a 50  $\Omega$  impedance from the diamond to the cable.

A preliminary test of a CVD diamond PCD to record the x-ray bang showed the necessity of reducing the background.<sup>8</sup> The x-ray signal from the 840-kJ NIF shot N091030 had the strongest bang signal-to-background ratio recorded by this diagnostic but the signal was a factor of  $\sim 7\times$  smaller than the background signal. Since subsequent higher laser power NIF

shots were anticipated to have much higher background x rays, the SPBT was designed to maximize the x-ray bang signal-to-background contrast in two ways: the diagnostic view of the background x-ray source is minimized and crystal monochromators select the optimum x-ray energy.

The background signal from a NIF hohlraum implosion is primarily a result of x rays coming from the hohlraum's inside wall due to thermal radiation and bremsstrahlung radiation induced by fast electrons from laser-plasma interactions. SPBT reduces this background by minimizing its view of the hohlraum's inside wall. The diagnostic head is positioned on the hohlraum's south polar axis placing the detectors at  $z = -316$  cm from target chamber center (TCC) with a view of the capsule implosion through the LEH of the hohlraum, as shown in Fig. 3.

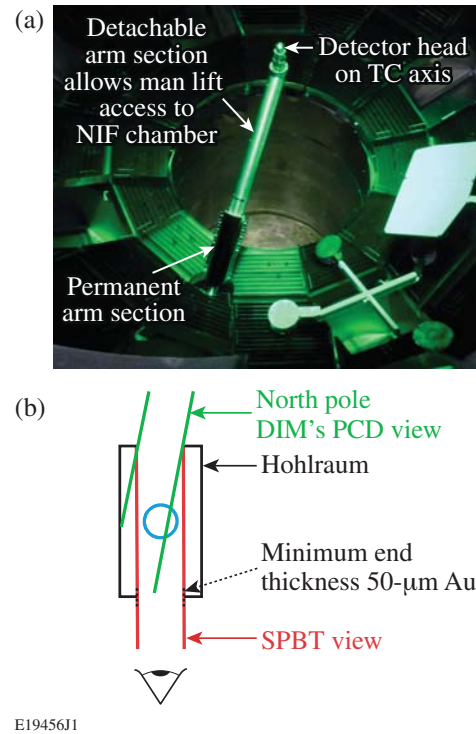
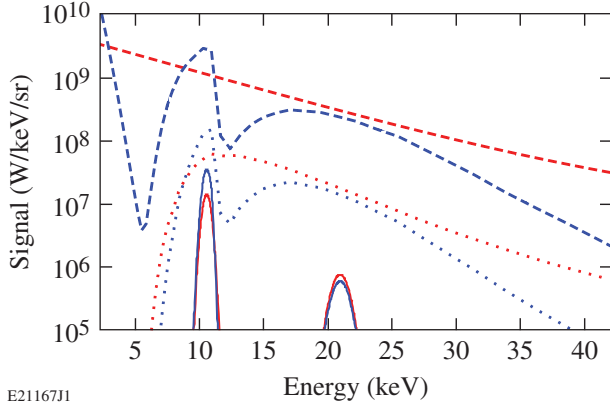


FIG 3. (a) The SPBT is installed in the NIF with the detector head on the target chamber's south polar axis viewing upward. The SPBT detector head is mounted to the target chamber on the end of a metal arm. The upper part of the arm is removable to allow one access into the NIF target chamber via a man-lift. (b) SPBT on-axis view (red) through the lower laser entrance hole (LEH) ensures that the only part of the hohlraum's inside wall directly seen by the diagnostic is the opposite LEH rim.

A small portion of the opposite LEH rim is the only inside portion of the hohlraum directly viewed by the diagnostic [see Fig. 3(b)]. SPBT is shielded from the rest of the hohlraum's inner wall by a minimum of 50  $\mu\text{m}$  of gold in the hohlraum's end wall. Collimating the view further was not considered to keep the alignment tolerances loose and avoid *in-situ* adjustments.

SPBT was designed to further improve the signal-to-background contrast by incorporating monochromators to select x rays where the capsule x-ray brightness was predicted to be maximized with respect to the x-ray background. Figure 4 shows that a peak exists in the simulated x-ray spectrum during the capsule bang around 10 keV predicted by the radiation-hydrodynamics code LASNEX.<sup>11</sup> The background spectrum for a

NIF hohlraum implosion was inferred from the time-integrated filter-fluorescer x-ray diagnostic system (FFLEX)<sup>12</sup> data measured for an equivalent shot. This broadband background spectrum is stronger than the predicted capsule spectrum except near 10 keV and below 3 keV, where thermal x rays not visible to FFLEX will increase the background levels.



E21167J1

FIG 4. Predicted x-ray source spectra for a 1-MJ layered cryogenic shot. The LASNEX-predicted spectra from the capsule (dashed blue)<sup>11</sup> has a peak around 10 keV, where it is stronger than the background spectra (dashed red) estimated from FFLEX<sup>12</sup> data. The solid and dotted lines show the estimated x rays absorbed in the PCD with and without the HOPG mirror (respectively). The integrated spectrum of the capsule will be greater than the integrated background only with the HOPG.

Highly ordered pyrolytic graphite (HOPG) crystals with an  $0.8^\circ$  mosaic spread oriented to select 11 keV have been placed in the x-ray path on four of the five SPBT PCD's. This specific x-ray energy band allows SPBT to use the second-order reflection to detect silver  $K_\alpha$  x rays at 22 keV generated during NIF timing calibration shots (see Sec. IV). One drawback of this energy band is that it straddles the Ge K-edge and the x-rays bang spectrum above the edge is significantly reduced by absorption for capsules with Ge doping.<sup>13</sup> This K-edge absorption has not prevented SPBT from successfully measuring x-ray bang peaks from Ge-doped capsule implosions. The size of the HOPG crystals ( $12 \times 48 \times 1$  mm) ensures that the reflected x rays overfill the PCD detector areas to ameliorate any slight misalignments in mounting the diagnostic.

The PCD's and HOPG mirrors are encased in a detector head made of the tungsten alloy hevimet<sup>14</sup> to shield them from stray x rays. Redirecting the x rays via a HOPG mirror reduces unwanted background signals in two ways: First, those PCD's have no direct line of sight with any high-atomic-number material directly exposed to x rays from TCC and are shielded from fluorescence. Secondly, it allows a sufficient amount of hevimet shielding to be placed between the PCD and TCC to block neutron-induced high-energy gammas from the implosion.

The detector head is supported by a fixed arm as shown in Fig. 3(c). The inner half of this support arm and the detector head are a line replaceable unit (LRU) that can be removed and replaced, facilitating swapping in new PCD's or filters if needed. The LRU must be temporarily removed if the man-lift at the bottom of the target chamber is used for personnel access to the chamber's interior. The support arm provides additional electromagnetic interference (EMI) shielding for the cables connecting the detectors with the electronics located just outside

the target chamber. There are at least two layers of EMI shielding around the detectors and cables inside the NIF target chamber.

The high-voltage power supplies and bias-tees used to bias the PCD's at their  $-1500$ -V operating voltage are located just outside the target chamber. The detector signals travel approximately 40 m via 12-GHz-bandwidth LMR600 cable<sup>15</sup> to the NIF diagnostic mezzanine where they are recorded. Currently a Tektronic DPO70604 scope<sup>16</sup> records four of the five available detector channels on NIF target shots with a 40-ps sampling time. Three of those four channels are simultaneously recorded by fast transient FTD10000 digitizers<sup>17</sup> with a 10-ps sampling time. At the current level of implosion performance on the NIF, the main SPBT data channel is the FTD10000 record of the most-sensitive HOPG reflected PCD. This data channel is used in the discussion for the remainder of this paper unless otherwise noted.

### III. DATA PROCESSING

For each NIF shot, in addition to the detector signal image, both pre-shot and post-shot images of a zero-voltage baseline streak are recorded. First, each of these three images is background adjusted by subtracting a "dark" image from each shot. Next, the trace in each of the images is read using an algorithm developed by one of the authors (MacPhee), that produces fewer glitches and better subpixel resolution than the native scope readout. For each sample time (vertical line of image pixels), the location of the trace is determined from the "center of mass" in the trace intensity, over a narrow window about the intensity maximum. After the traces have been read, the detector data trace is baseline adjusted by subtracting the average of the pre-shot and post-shot waveforms.

The FTD10000 scope operates similarly to a streak camera. The time-varying signal modulates an electric potential through which an electron beam passes while being swept across a phosphor screen. The modulated potential creates a time-varying deflection of the electron beam on the screen proportional to the strength of the time-varying signal. A charge-coupled-device (CCD) camera in the scope records an image of the screen. The advantages of the FTD10000 include its fast 10-ps sample time and its resistance to overvoltage damage (required in case of an accidental discharge of the  $-1500$ -V bias voltage). A major disadvantage of the FTD10000 is that, like a sweep camera, the speed of the sweep rate across the image is not constant.

The sweep speed of an FTD10000 scope can be measured by recording the streak of an oscillating signal of fixed and known frequency. We record a 4-GHz signal and measure the position of the rising and falling midpoints in the signal. The distance between consecutive rising midpoints (or falling points) is equal to one period of the signal. By treating the rising and falling midpoints as separate sets of data, we prevent any non-sinusoidal variation in the signal from affecting our calibration. The results of three independent measurements of the sweep speed for an FTD10000 scope are shown in Fig. 5. The variation in sweep speed across the sweep is reproducible trace to trace. Even though some high-order variation in the sweep speed is reproduced in all three calibrations, the scatter is too large to justify fitting this high-order structure. Instead, a sixth-order polynomial is fit to the sweep-speed variation. The average of the three fits is used as the scope time calibration.

The amplitude of the trace is converted from pixels to detector voltage using the scope sensitivity adjusted for any attenuation. The nonlinearity in the detector response caused by the finite bias voltage is compensated using,<sup>18</sup>

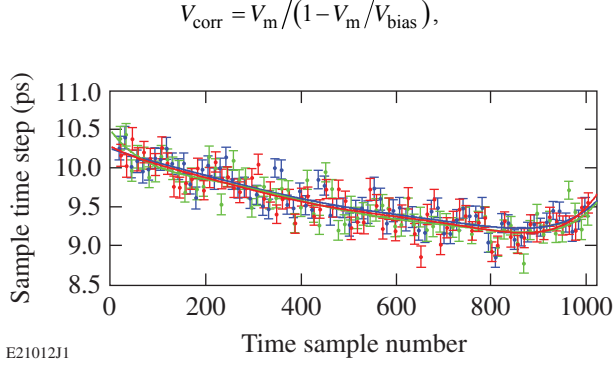


FIG 5. The time step between sample points varies over the FTD10000 sweep. The data points (with error bars) were determined from the period of a 4-GHz signal. Each color represents an independent measurement. The solid lines are  $n = 6$  polynomial fits to the data sets.

where  $V_{\text{bias}}$  is the detector bias voltage,  $V_m$  is the measured signal voltage, and  $V_{\text{corr}}$  is the corrected signal voltage. Typically, this correction is very small as  $V_m \ll V_{\text{bias}}$  but will become more important as ignition is approached and bang signals increase.

Next, the temporal instrument response function (tIRF) is deconvolved from the measured detector signal to produce a signal that is proportional to the true time-varying intensity of the x-ray energy absorbed in the detector. The tIRF is the system's time-varying response to an impulse. Details of how we determined the tIRF for this detector are given Sec. IV.

The iterative deconvolution method of Nagy and Strakoš<sup>19</sup> is used. It uses a modified steepest decent algorithm to minimize the least-squares difference between the measured signal and the convolution of the deconvolved signal with the tIRF subject to the constraint that the deconvolved signal must be  $\geq 0$ . Applying this nonnegativity constraint at each iteration prevents unphysical negative x-ray intensities in the deconvolved signal.

#### IV. ANALYSIS OF A TIMING SHOT

To determine the SPBT signal's true timing with respect to the NIF laser pulse, the FTD10000 sweep time must be correlated to the NIF system timing. By inserting an optical fiducial pulse into the SPBT signal, we can infer the timing of the instrument using an SPBT x-ray timing shot (see Fig. 6). The timing shots use the shortest laser pulse available on the NIF, an 88-ps impulse, on each NIF quad. The laser impulses irradiate a planar silver target at TCC and produce a short burst of 22-keV  $K_\alpha$  x rays. The time history of the x-ray burst can be assumed to be very similar and concurrent to the laser pulse whose timing with respect to the NIF reference time ("system  $t_0$ ") is measured by NIF's Laser Performance Operations Model.<sup>20</sup> By measuring the time of the x-ray peak in the deconvolved data trace, and the fiducial pulse, we determine the absolute timing of the SPBT fiducial with respect to the NIF system  $t_0$  to be

$$\Delta t_{0 \rightarrow f} = (t_f - \Delta t_s - \delta t_f) - (t_x - \Delta t_x - \delta t_r) + \Delta t_L,$$

where  $t_f$  is the measured fiducial time (statistical error  $\approx 5$  ps);  $\Delta t_s$  is the delay in the fiducial related to its cable (systematic error  $\approx 1$  ps);  $\delta t_f$  is the error in the fiducial caused by jitter (statistical error  $\approx 3$  ps);  $t_x$  is the measured x-ray pulse time (statistical error

from a deconvolution procedure  $\approx 10$  ps, systematic error from uncertainties in tIRF  $\approx 10$  ps, and systematic error from

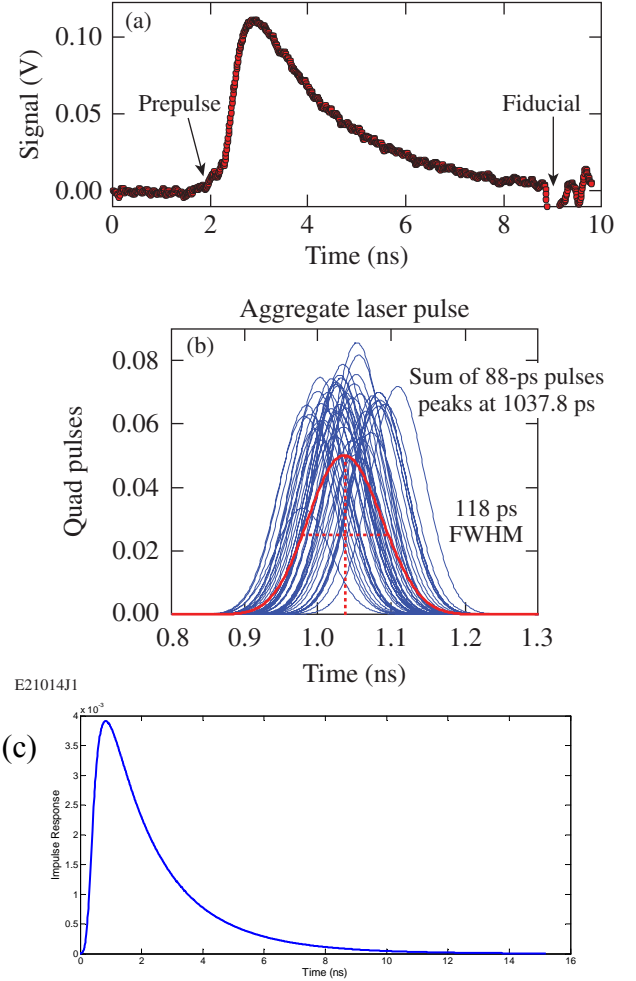


FIG 6. Analysis of a timing shot. (a) The signal trace from a recent NIF SPBT timing shot. The prepulse is due to a relatively weak 1-ns square laser pulse used to create a plasma at the target before the main laser impulse. (b) The shape of the total laser impulse is the aggregate of 88-ps impulse for each NIF laser quad. (c) The temporal instrument response function (tIRF) inferred by deconvolving the laser pulse shape from the measured SPBT signal for a timing shot (normalized to conserve collected charge).

uncertainties in sweep-speed correction  $\approx 9$  ps);  $\Delta t_x$  is a possible delay in the x-ray pulse with respect to laser incidence (systematic error  $\approx 5$  ps);  $\delta t_f$  is the error in x-ray pulse arrival time caused by a target-positioning error (statistical error  $\approx 3$  ps); and  $\Delta t_L$  is the offset in the laser-arrival time from system  $t_0$  (statistical error  $\approx 6$  ps). Summing in quadrature the statistical and systematic terms separately gives 14-ps statistical error and 15-ps systematic error for a total estimated error in  $\Delta t_{0 \rightarrow f}$  of 29 ps.

We use the SPBT x-ray timing shots to infer the *in-situ* tIRF of the SPBT detector. The system's tIRF must be accurately known or the deconvolution could produce inaccurate and unphysical results. The tIRF's of the SPBT detectors were measured offline<sup>8</sup> prior to their installation on the NIF using ultrashort x-ray pulses produced by the COMET laser, part of the Jupiter Laser facility<sup>21</sup> at LLNL. After installation, the *in-situ*



decay times of the detector's signals proved longer than the decay times of the offline-measured tIRF's. Deconvolution using the offline tIRF's showed a false long-term background x-ray signal during the signal's decay. This had a small effect on the measured bang time but significantly affected the measurement of x-ray yield.

Since the x-ray pulse can be assumed to have a time history similar to the laser pulse, the *in-situ* tIRF is determined by deconvolving the known x-ray time history from the measured signal of an SPBT timing shot (as opposed to the normal deconvolution of the known tIRF from a measured signal to produce the true time-varying signal).

As noise fluctuations in the measured signals occur on a much-faster time scale than the response time of the detector's tIRF, they can produce large fluctuations in deconvolved data despite the small amplitude of the noise. Smoothed data is used to prevent this from marring the inferred tIRF's.

The measured detector signal from a timing shot is shown in Fig. 6(a) along with its smoothed version. A smoothing spline is used for the rising edge and the peak of the signal. The signal's falling edge is fit to a single or double exponential decay.

A smooth laser pulse suitable for use in deconvolution is constructed from the sum of 88-ps FWHM Gaussian impulses from each laser quad. While all laser quads have identical setups in a timing shot, the actual impulse from each quad will have a slightly different power and will arrive at a slightly different time. We use the measured quad powers and arrival times for the timing shot to construct an aggregate laser pulse, as shown in Fig. 6(b). The tIRF for the SPBT detector inferred from this deconvolution is shown in Fig. 6(c).

## V. ANALYSIS OF THE BANG-TIME PEAK

Once the SPBT signal from a NIF capsule implosion has been deconvolved and the timing has been correlated with the NIF laser pulse, the x-ray bang peak is inferred. The bang-time peak is usually easily discriminated from the decaying background signal, as shown in Fig. 7. Discriminating the background signal from the bang peak can be more difficult in implosions with longer laser pulses or if an x-ray backlighter provides a strong time-varying x-ray source of unknown time history that overlaps the bang peak. These shots must be dealt with on a case-to-case basis.

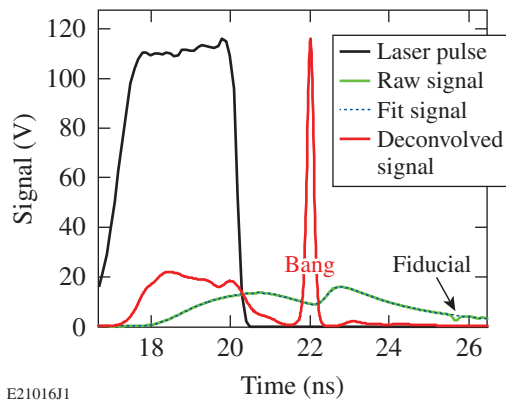


FIG 7. Sample SPBT signal for a NIF implosion. The fit signal (blue) is formed by the convolution of the tIRF with the deconvolved signal (red) and is a good reconstruction of the original data (green). The laser pulse shape (black) is shown for reference.

Once the background has been removed, the bang peak (see Fig. 8) can be analyzed for its peak time (x-ray bang time), FWHM (bang width), and total area (bang yield). Model predictions of the x-ray bang peak are typically skewed and not true Gaussian peaks. Since the x-ray bang time is defined as the time of peak x-ray emission, the SPBT bang peak is determined with subpixel precision by spline interpolation over the highest points of the deconvolved x-ray peak. The error in the measurement is estimated by examining all the terms that contribute the timing calculation of the bang time:

$$t_{BT} = \Delta t_{0 \rightarrow f} - (t_f - \Delta t_s - \delta t_f) + (t_x - \Delta t_a - \delta t_r) - \Delta t_L,$$

where  $\Delta t_{0 \rightarrow f}$  is the timing-shot calibration (systematic error of 29 ps) and  $\Delta t_a$  is the delay in the x-ray signal related to its up-to-three attenuators (statistical error  $\approx 1$  ps each). The rest of the terms and errors are the same as in Sec. IV except that the systematic error from uncertainties in the sweep-speed correction is only 3 ps because we are concerned only with the portion of the streak where the bang signals are recorded. This gives a 14-ps statistical error and a 31-ps systematic error for a 45-ps total estimated error in the bang time. Figure 9 compares the SPBT bang times with those measured by GXD and hGXI. They typically agree within the error bars of the diagnostics.

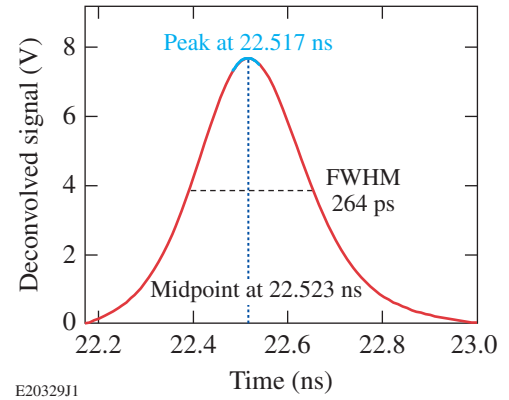


FIG 8. Analysis of the bang peak. The bang time (time of the maximum signal) is several ps different from the midpoint of the peak.

The bang width is the FWHM of the bang peak. This quantity is often referred to as the x-ray “burn width,” which is technically incorrect since the x-ray bang peak does not come from nuclear burn. At present, SPBT cannot reliably measure the x-ray bang width. Studies of the SPBT signal deconvolution have shown that as deconvolution is carried out for more and more iterations, the bang peak's FWHM will shrink to an unphysically narrow peak, even though the position of the bang peak remains unchanged by more than a few picoseconds. This is believed to be related to uncertainty in the tIRF and efforts are undergoing to reliably resolve the x-ray burn width.

Since the tIRF is constructed to conserve the total signal, the area under the bang peak remains a valid parameter even when the FWHM is not. This total area, or, equivalently, the total charge from the current through the PCD, is proportional to the total x-ray energy absorbed by the diamond detector and is a measure of the x-ray bang “yield” defined as the time-integrated spectral radiant intensity (mJ/sr/keV) at 11 keV.

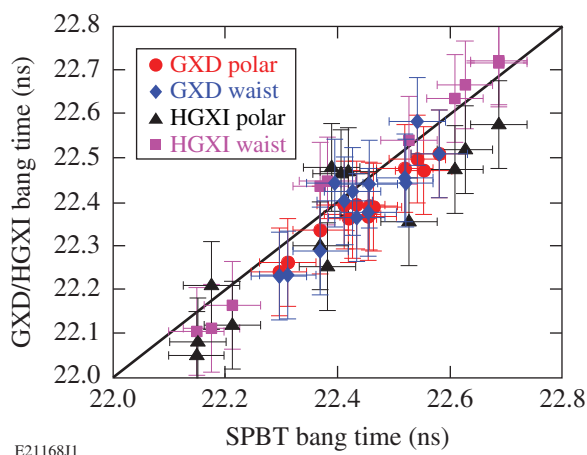


FIG 9. The bang times measured by SPBT are compared with those from the gated x-ray detector (GXD) and hardened gated x-ray imager (HGXI) for many NIF implosions.

The absolute sensitivity for a CVD diamond similar to the one in the main SPBT channel was calibrated at the LBNL's Advanced Light Source (ALS)<sup>22</sup> cyclotron. The ALS emitted short "bunches" of 10.8-keV x-rays at a rate of  $3.05 \times 10^6$  bunches per second. The ALS-calibrated reference diode detector measured the exposure level as  $1.2 \times 10^{12}$  photons/s. The diamond PCD, biased at  $-1500$  V, was exposed to the ALS x rays and the response from a single bunch ( $3.9 \times 10^5$  10-keV photons or 0.67 nJ) was recorded on an FTD10000 scope. The total collected charge obtained by integrating the scope trace was 2.0 coulombs, giving a detector sensitivity of 3.0 mC/J (or, equivalently, 3.0 mA/W). The error on this sensitivity is dominated by a 27% error in the ALS diode calibration. Since the actual CVD diamonds deployed in the NIF chamber cannot be calibrated, an additional 25% error for the variation in sensitivity between similar diamonds must be added in quadrature for an estimated error of  $\pm 37\%$  on the diamond-sensitivity calibration.

To calculate the SPBT detector calibration factor, the detected coulombs are converted into an x-ray yield (in J/sr/keV) following the procedure in Ref. 23. This gives a factor for the x-ray yield at 11 keV of  $1.8 \times 10^9$  J/sr/keV/ $C \pm 50\%$ . The largest contributors to this error are systematic and fixed for a given detector. The error bars will be much smaller when comparing shot-to-shot yields from the same detector.

HYDRA<sup>24</sup> calculations show that the x-ray yield at 11 keV is a sensitive function of fuel velocity and the SPBT bang yields may be useful for inferring fuel velocity when there are no other measurements.<sup>25</sup>

The CVD diamond detectors are sensitive to the neutrons from the capsule bang, giving SPBT the potential to be used as a neutron diagnostic as well as an x-ray detector. The central SPBT channel, which has no HOPG mirror, is intended for neutron measurements, but the central channel CVD diamond currently installed in SPBT has insufficient sensitivity to make accurate neutron measurements. In principle we should be able to measure the neutron bang time with a higher-sensitivity diamond or larger neutron yields from the NIF implosions, but the tIRF for the neutron signal must include Monte Carlo modeling of the neutron scattering in the detector. We may also be able to measure the neutron down-scattered fraction with SPBT, an important measurement useful in calculating the  $\rho R$  of the capsule at bang time. This is a difficult measurement and will require careful analysis.

## VI. SUMMARY

The south pole bang-time has been deployed on the NIF to measure the time of peak x-ray emission from the capsule in indirect-drive implosions. Five CVD diamond PCD's with different filtrations and sensitivities measure the time-varying x rays emitted by the target. After signal deconvolution and background removal, the bang time is determined to 45-ps accuracy. The x-ray yield (mJ/sr/keV at 11 keV) is determined from the total area under the peak. Signal-to-background contrast is maximized by viewing the capsule directly along the NIF's south polar axis through the lower LEH and using HOPG crystal mirror monochromators to select 11-keV x rays. Laser impulse shots calibrate SPBT's in-situ timing and temporal instrument response function.

## ACKNOWLEDGMENT

This work was supported by the U.S. Department of Energy Office of Inertial Confinement Fusion under Cooperative Agreement No. DE-FC52-08NA28302, the University of Rochester, and the New York State Energy Research and Development Authority. This work performed under the auspices of the U.S. Department of Energy by Lawrence Livermore National Laboratory under Contract DE-AC52-07NA27344. The support of DOE does not constitute an endorsement by DOE of the views expressed in this article.

## REFERENCES

- <sup>1</sup>J. D. Lindl, *Inertial Confinement Fusion: The Quest for Ignition and Energy Gain Using Indirect Drive* (Springer-Verlag, New York, 1998).
- <sup>2</sup>E. I. Moses, *Fusion Sci. Technol.* **44**, 11 (2003).
- <sup>3</sup>J. D. Lindl, *Phys. Plasmas* **2**, 3933 (1995).
- <sup>4</sup>J. A. Oertel *et al.*, *Rev. Sci. Instrum.* **77**, 10E308 (2006).
- <sup>5</sup>S. Glenn *et al.*, *Rev. Sci. Instrum.* **81**, 10E539 (2010).
- <sup>6</sup>P. M. Bell *et al.*, *Rev. Sci. Instrum.* **81**, 10E540 (2010).
- <sup>7</sup>Ref to SPIDER to come from Dana???
- <sup>8</sup>A. G. MacPhee *et al.*, *J. Inst.* **6**, P02009 (2011).
- <sup>9</sup>G. J. Schmid *et al.*, *Rev. Sci. Instrum.* **74**, 1828 (2003).
- <sup>10</sup>V. Yu. Glebov, C. Stoeckl, T. C. Sangster, C. Mileham, S. Roberts, and R. A. Lerche, *Rev. Sci. Instrum.* **77**, 10E712 (2006).
- <sup>11</sup>C. J. Cerjan, LLNL, private communication (2011).
- <sup>12</sup>J. W. McDonald, R. L. Kauffman, J. R. Celeste, M. A. Rhodes, F. D. Lee, L. J. Suter, A. P. Lee, J. M. Foster, and G. Slark, *Rev. Sci. Instrum.* **75**, 3753 (2004).
- <sup>13</sup>S. P. Regan *et al.*, *Phys. Plasmas* **19**, 056307 (2012).
- <sup>14</sup>Tungsten Alloy HD17 (90% W, 6% Ni, 4% Cu), Mi-Tech Metals, Inc., accessed 27 April 2012, <http://www.mi-techmetals.com/hd-typical.htm>.
- <sup>15</sup>Times Microwave Systems, accessed 26 April 2012, [www.timesmicrowave.com/products/lmr/downloads/28-31.pdf](http://www.timesmicrowave.com/products/lmr/downloads/28-31.pdf).
- <sup>16</sup>Tektronix, Inc., accessed 26 April 2012, <http://www.tek.com>.
- <sup>17</sup>Greenfield Technology, accessed 26 April 2012, [www.greenfieldtechnology.com/IMG/pdf/FTD10000.pdf](http://www.greenfieldtechnology.com/IMG/pdf/FTD10000.pdf).
- <sup>18</sup>D. R. Kania, L. S. Pan, P. Bell, O. L. Landen, H. Kornblum, P. Pianetta, and M. D. Perry, *J. Appl. Phys.* **68**, 124 (1990).
- <sup>19</sup>J. Nagy and Z. Strakoš, in *Mathematical Modeling, Estimation, and Imaging*, edited by D. C. Wilson, H. D. Tagare, F. L. Bookstein, F. J. Prêteux, and E. R. Dougherty (SPIE, Bellingham, WA, 2000), Vol. 4121, p. 182.
- <sup>20</sup>M. Shaw, R. House, W. Williams, C. Haynam, R. White, C. Orth, and R. Sacks, *J. Phys., Conf. Ser.* **112**, 032022 (2008).
- <sup>21</sup>Jupiter Laser Facility, accessed 26 April 2012, <https://jlf.llnl.gov/>.
- <sup>22</sup>Advanced Light Source, accessed 26 April 2012, <http://www-als.lbl.gov/>.
- <sup>23</sup>B. Henke, H. Yamada, and T. Tanaka, *Rev. Sci. Instrum.* **54**, 1311 (1983).
- <sup>24</sup>M. M. Marinak, S. W. Haan, T. R. Dittrich, R. E. Tipton, and G. B. Zimmerman, *Phys. Plasmas* **5**, 1125 (1998).
- <sup>25</sup>D. A. Callahan *et al.*, *Phys. Plasmas* **19** (5), 056305 (2012).